

Zigzag charged domain walls in ferroelectric PbTiO₃Pavel Marton ^{1,2,*}, Mauro A. P. Gonçalves ¹, Marek Paściak ¹, Sabine Körbel ^{1,3}, Věnceslav Chumchal ⁴,
Martin Plešinger ⁴, Antonín Klíč ¹ and Jirka Hlinka ¹¹*Institute of Physics, Czech Academy of Sciences, Na Slovance 2, 182 00 Praha 8, Czech Republic*²*Institute of Mechatronics and Computer Engineering, Technical University of Liberec, Studentská 2, 461 17 Liberec, Czech Republic*³*Institute of Condensed Matter Theory and Solid State Optics, Friedrich Schiller University Jena, Max-Wien-Platz 1, 07743 Jena, Germany*⁴*Department of Mathematics and Didactics of Mathematics, Technical University of Liberec, Studentská 2, 461 17 Liberec, Czech Republic*

(Received 10 November 2022; revised 7 February 2023; accepted 16 February 2023; published 6 March 2023)

We report a theoretical investigation of a charged 180° domain wall in ferroelectric PbTiO₃, compensated by randomly distributed immobile charge defects. For this we utilize atomistic shell-model simulations and continuous phase-field simulations in the framework of the Ginzburg-Landau-Devonshire model. We predict that domain walls form a zigzag pattern and we discuss their properties in a broad interval of compensation-region widths, ranging from a couple to over 100 nm. The zigzag is accompanied by a local polarization rotation which we explain to provide an efficient mechanism for charge compensation.

DOI: [10.1103/PhysRevB.107.094102](https://doi.org/10.1103/PhysRevB.107.094102)**I. INTRODUCTION**

Ferroelectric materials are known to host complicated domain structures that can be used to tune the material properties for a specific application. It turns out that interfaces between the domains—the domain walls—have very different properties, e.g., electrical conductivity [1,2] or phonon modes [3], from the bulk ferroelectric itself, and therefore understanding the microstructure of the domain wall is receiving increasing attention in the research of ferroelectrics.

The domain walls are typically electrically neutral or near neutral, i.e., $(\mathbf{P}_1 - \mathbf{P}_2) \cdot \mathbf{n} \approx 0$, where \mathbf{P}_1 and \mathbf{P}_2 are the ferroelectric polarizations inside the ferroelectric domains on either side of the wall of interest, and \mathbf{n} is the wall normal. This is because deviation from the charge-neutrality condition leads to a large energy penalty due to the depolarizing electric fields from the polarization-originated bound charges $q_P = -\text{div}\mathbf{P}$ at the walls. In a perfect dielectric material these depolarization fields would suppress charged interfaces in the early stages of their formation.

However, in spite of apparently unfavorable electrostatics, charged ferroelectric domain walls do exist [4–7]. This can be rationalized by the presence of charged defects such as, e.g., electrons, or ionic-type point defects, which compensate for the charge of such walls. The charged walls, as they usually involve defects of some kind, are different compared to their neutral counterparts, and therefore exhibit different properties (such as, e.g., electric conductivity [8] and potentially enhanced dielectric response functions [9]); this makes them interesting from both fundamental and application perspectives.

Charged domain walls have been studied theoretically using analytical considerations and model Hamiltonians

[10–12], density-functional theory [13–15], and phase-field simulations [9,16–18], demonstrating the richness of exciting phenomena associated with the charged-domain-walls physics, including enhancement of the piezoelectric and dielectric response of a material hosting such walls, differences in the mobility of charged walls compared to their neutral counterparts, as well as various, sometimes rather complicated domain-wall configurations. A common feature of the previous studies is that the compensation charges, if considered, are localized in the domain wall, or in a very narrow region close to the wall, i.e., the focus there is on defects that can migrate towards the charged wall, or materialize during the wall formation. However, the compensating charges might not be able to migrate easily and can be distributed over a much broader region than considered so far. Such charge configuration is poised to have an impact on the form and functionality of the domain wall.

Therefore, in this paper we address a situation with static compensation-defect charges distributed over a relatively wide region. We combine shell-model and phase-field simulations to study the microstructure and properties of a domain wall with a charge-compensation region thickness up to 100 nm. This multiscale approach allows us to consider a large system in the phase-field simulation while maintaining the accuracy of the atomistic shell model, which is limited to smaller system sizes. We concentrate on the 180° tail-to-tail domain wall in PbTiO₃ (PTO), a well-known ferroelectric material, for which parameters are available in the literature for both shell-model and phase-field simulations.

In Sec. II we provide details of the utilized methodology; in Sec. III we review the results obtained using shell-model and phase-field simulations, which are discussed in detail in Sec. IV, where we also provide a simplified model explaining the observations. Finally, the paper is concluded in Sec. V.

*marton@fzu.cz

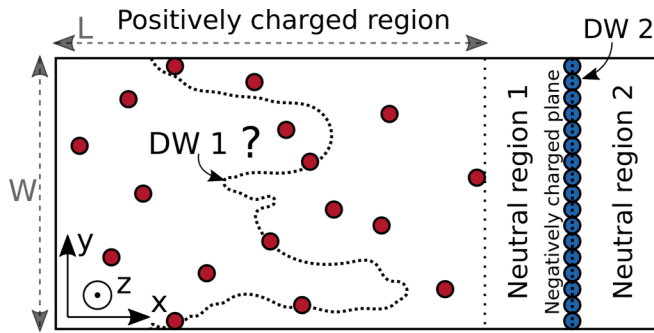


FIG. 1. Sketch of distribution of charged-wall-compensation charges in the x - y cross section of the simulation box. Positive charges (red) are distributed randomly in a layer of thickness L (region of interest in simulations); negative charges (blue) are located on a plane. The charged regions are separated by neutral regions. The electrostatics dictates that two domain walls will develop: A tail-to-tail domain wall (DW1) in the positively charged region, and a head-to-head wall (DW2) in the negatively charged plane. The properties and location of the DW1 are not known *a priori* and are the subject of this study, while the DW2 is collocated with the negatively charged plane.

II. METHOD

A. Supercell

The cross section of the all-periodic supercell utilized for the calculations is schematically depicted in Fig. 1. Along the direction x , it consists of two neutral areas, separated by positive and negative compensation charges distributed in broad and very narrow (planar) regions, respectively. The charges are chosen to exactly compensate for the head-to-head and tail-to-tail 180° domain walls, and they sum up to zero. It follows from the electrostatic considerations that the two neutral regions will host oppositely oriented ferroelectric polarization, separated by two charged 180° domain walls located inside the charged regions.

The negatively charged tail-to-tail wall (DW1), which is of interest in this work, is expected to form within the thick positively charged compensation layer covering most of the simulation box. The positive charges in this wall have average yz -planar density $\sigma_{DW1} = 2P_s$, and are distributed randomly. The position and shape of the wall DW1 are not restricted in any other way, so it is not *a priori* clear whether the wall is going to be thick or narrow, planar, or will adopt some more complicated profile.

The positively charged head-to-head wall (DW2) is on the right-hand side of the box and forms within a negatively charged compensation layer with the charge density of $\sigma_{DW2} = -2P_s$. This wall is not of particular interest in this work and is only present as a consequence of the simulation-box periodicity. Therefore, this compensation layer is prepared as thin as possible.

Notice that both present domain walls DW1 and DW2 are charged, but at the same time the region of either wall is electrically neutral: The polarization-originated bound charges are exactly balanced by the compensation (defect) point charges. By calling a wall positive or negative, it is always referred to as its bound charge due to the head-to-head or tail-to-tail

arrangement of the ferroelectric polarization in the adjacent domains.

The simulation box is, in general, three dimensional. While the x dimensions of both neutral regions and the DW2 remain constant in all simulations, we alter the thickness L of the charged region and the y dimension of the simulation box W . Notice that the periodic boundary conditions in all directions imply, in particular, the periodicity of polarization and electric fields.

B. Shell-model setup

For atomistic simulations we used a shell model potential [19] for a solid solution of PbTiO_3 and $\text{PbMg}_{1/3}\text{Nb}_{2/3}\text{O}_3$ with parameters fitted to first-principles results [20]. Therein the atomic charges (core + shell) are treated as parameters and attain the following values: $\text{Pb}^{+1.80}$, $\text{Ti}^{+2.88}$, $\text{O}^{-1.56}$, $\text{Mg}^{+2.36}$, $\text{Nb}^{+3.15}$. The spontaneous polarization obtained for pure PTO using this model is $P_s = 0.66 \text{ Cm}^{-2}$. Notice that working within an atomistic approach requires the use of defined substituting atoms. Our choice of Mg and Nb is motivated by the appropriate charge provision and parametrization that is proven to work in the PbTiO_3 environment [20]. Nevertheless, the use of particular species is not expected to curtail a general result on the charged 180° DW (as indeed confirmed by the phase-field calculations).

The model allows us to study the simulation box described above (Fig. 1), with the DW1 layer ($L = 48$ unit cells) having a fraction of Ti atoms randomly substituted by a Nb and DW2 layer (two unit cells thick) with all Ti atoms replaced by Mg. The two neutral regions are seven unit cells thick and the total size of the supercell is $64 \times 44 \times 6$ unit cells.

To optimize atomic positions we run molecular dynamics simulations at low temperature ($T = 1 \text{ K}$) using the DLPOLY software [21]. The time step was 0.4 fs. The atoms in the initial configuration were in their ideal cubic positions. The neutral region is under an electric field due to the charged layers, therefore in each neutral region, the polarization develops parallel to the electric field to which it is subject. After equilibration for 30 ps, a trajectory of 10 ps was collected and used for calculation of various properties of interest.

Finally, in the simulations the system is mechanically free in all directions, which implies that all dimensions of the supercell can vary during the simulation time. To understand the implications of this approach, we also performed calculations imposing the tetragonal strain of PTO (bigger lattice parameter along x). When comparing the results of the two approaches it is evident that constraining the lattice parameters has no substantial impact on the results.

C. Phase-field setup

The phase-field simulations are performed using the code FERRODO2 [22], which implements the evolution of the ferroelectric polarization in the framework of the Ginzburg-Landau-Devonshire model together with the dissipative Landau-Chaladnikov dynamics. Landau, gradient, elastic, electrostrictive, and electrostatic interactions are taken into account. For the exact form of the individual energy terms, see Ref. [23].

The utilized parametrization [24] of the local part of the energy functional for PTO is based on first-principles calculations and was obtained using the same procedure as described in Ref. [25]. Thus, the simulation temperature is 0 K, similar to the shell-model approach. The gradient interaction is chosen as isotropic. The spontaneous polarization resulting from this parametrization is $P_s = 0.80 \text{ Cm}^{-2}$ (notice that the spontaneous value differs from the shell model). We tested that the outcomes of the presented simulations do not particularly depend on the used parametrization and temperature, e.g., using the temperature-dependent Model I for PTO from Table 4.6 in Ref. [23] (@ $T = 298 \text{ K}$).

The defect charges are represented by point charges (thus, in contrast to the shell model they have no relation to a specific atomic species). For the sake of analytical derivations (see below) we also consider a homogeneous distribution of the compensation charge, which allows us to eliminate local effects related to the discrete nature of point charges. The interaction of the defect charges with the PTO is purely electrostatic and relies on explicitly solving the Laplace equation for the electric potential and subsequent evaluation of the local electric fields due to defect charges. The volume density of compensation charge is chosen as $2P_s/L$. When integrated along the x axis, it leads to the expected charge density $\sigma_{DW1} = 2P_s$ in the yz plane.

The spatial step Δ is chosen similarly to the lattice constant of PTO, $\Delta = 0.4 \text{ nm}$. We vary the thickness L of the positive compensation charge; both neutral regions have thicknesses of 20Δ ; DW2 is 2Δ thick.

The initial ferroelectric polarization was set to zero. For the homogeneous compensation charge a small perturbation was added, allowing the wall to depart from the strictly planar configuration, corresponding to an unstable, but symmetry-locked solution.

The system is mechanically free in all directions [26]. This choice allows us to be consistent with the shell model, where it is difficult to combine mechanical clamping and pressure for different components of the stress-strain boundary conditions. It was tested, however, that the use of such combined boundary conditions has only a minor impact on the results.

The energy functional utilizes the elimination of mechanical strain under the condition of mechanical equilibrium, i.e., the strains immediately follow the polarization [27]. Let us stress that in all simulations the polarization and strain are treated as fully three dimensional.

III. RESULTS

A. Shell-model simulations

The most important observation obtained from shell-model simulations is that the tail-to-tail domain wall develops into a zigzag wave inside the charged region, as depicted in Fig. 2(a). The domain wall itself (the transition region where the polarization reverses) is rather narrow irrespective of the thickness of the charged region: The polarization changes its orientation from negative to positive values within a couple of unit cells only. The zigzag triangles are not exactly symmetric, they are slightly skewed and have a fading, smokelike feature near

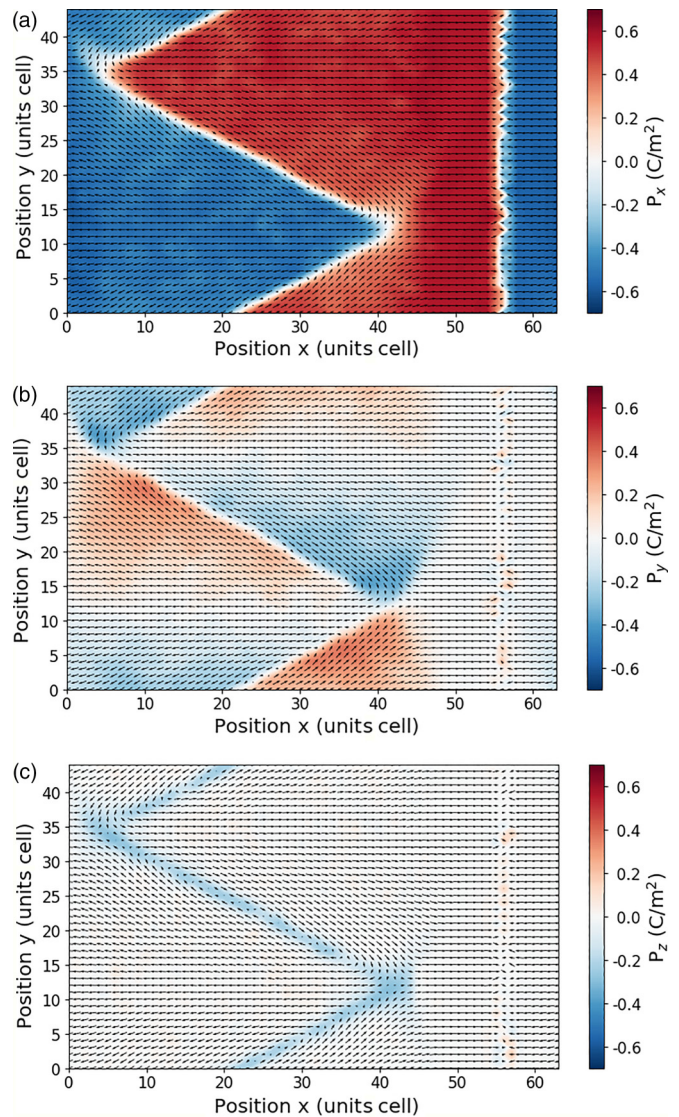


FIG. 2. A zigzag domain wall as obtained from shell-model simulations. Arrows stand for the polarization of individual unit cells projected to the xy plane, and color represents the P_x , P_y , and P_z components of polarization in individual panels. The domain wall in the figure was obtained for the $L = 48$ and $W = 45$ unit cells.

the top. The reasons for this deviation from ideal symmetric triangles will be addressed later.

Despite the significant difference between neutral and charged regions, we observe that the ferroelectric polarization exhibits no marked change at their interface. Instead, the domains from the neutral regions penetrate into the charged regions, with the P_x component remaining mostly unaffected.

Figure 2(b) shows the P_y . It is evident that this component of the polarization develops mainly in the triangular domains inside the charged regions. Its magnitude changes linearly along the y direction, going from negative to positive, and abruptly changes sign at the domain wall.

Figure 2(c) displays P_z , which is zero everywhere except for the domain wall, where both P_x and P_y are close to zero and instead P_z is finite.

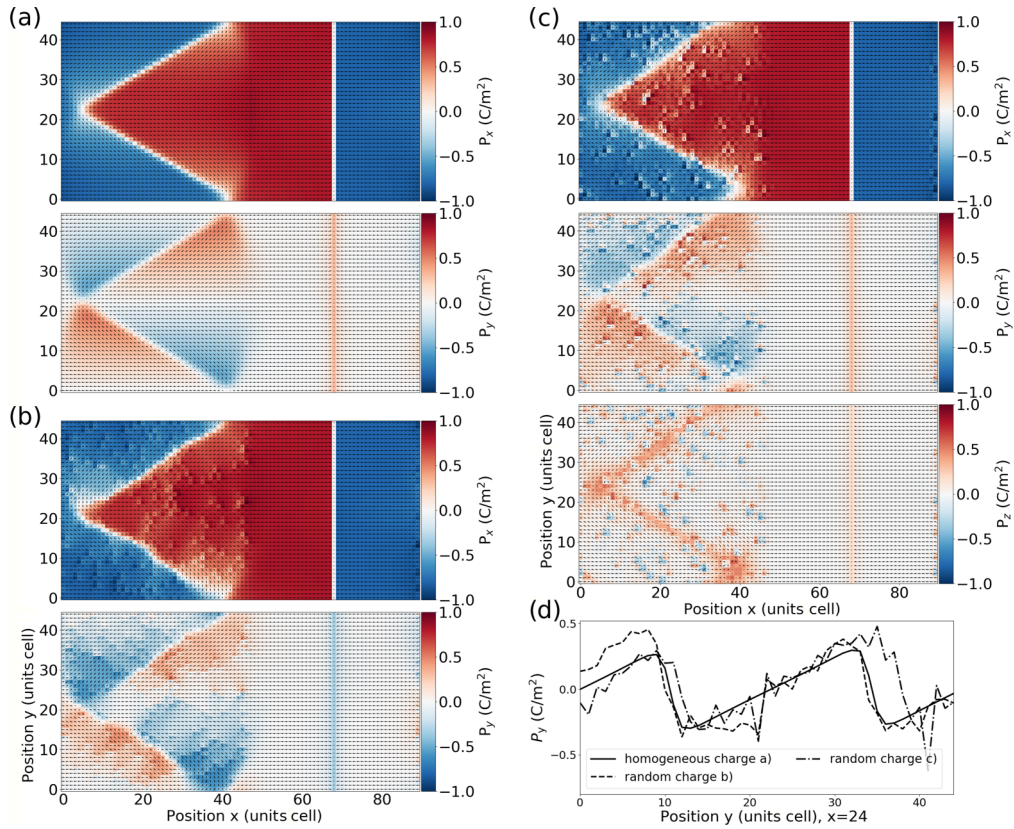


FIG. 3. A zigzag domain wall obtained from phase-field simulations. Three types of defect-charge distributions were considered, all of them leading to the same average charge density in the wall. (a) Homogeneous charge, (b) charges as in shell-model calculations, and (c) charges equal to the elementary charge. Color represents P_x and P_y in the first and second panel for each case [and P_z in the third panel of (c)]. d) $P_y(y)$ evaluated for $x = 24$ shows linear dependence inside the triangular domain for all three studied cases, and a steep decrease within the domain wall.

B. Phase-field simulations

The results obtained using the phase-field method are shown in Fig. 3. The dimensions L and W of the charged region are identical to those considered in the shell-model simulations (Fig. 2). The different overall dimensions of the xy -plane plots is caused by different thicknesses of the neutral regions: They are broader in the phase-field simulations than in the shell-model simulations. Three different ways of including the defect charges are considered. Figure 3(a) was obtained for a homogeneous distribution of the compensating charge and leads to a symmetric zigzag domain. The compensating charges in Fig. 3(b) are analogous to the compensating point charges used in the shell model. In Fig. 3(c) we used fewer point charges with a larger charge (the elementary charge $|e|$) [28]. Notice that the color scale slightly differs between Figs. 2 and 3, as the spontaneous polarization predicted by either model is different.

In accordance with the shell-model simulations, the dependence of the P_y on y within the triangular domain is approximately linear, as can be deduced from the corresponding panels of Figs. 3(a)–3(c). To demonstrate this more clearly, we plot the dependence of P_y along the y axis for all three studied compensation-charge distributions in Fig. 3(d). Clearly visible is the linear dependence of P_y inside the

triangular domain, and its rapid decrease in the region of the domain wall. Notice that $P_y = 0$ on the axis of the triangular domain.

The third panel in Fig. 3(c) displays the P_z component of the ferroelectric polarization. We observe an out-of-plane component in the region of the DW1, in agreement with the shell-model simulations (see the bottom panel of Fig. 2) [29]. A footprint of the tendency to form an extra component of polarization in the domain wall can be also observed in Figs. 3(a)–3(c) for the P_y component in the DW2 (for the head-to-head 180° DW2 the y and z directions are practically equivalent). The appearance of P_z in the charged wall is supported by auxiliary density-functional-theory calculations; its magnitude, nevertheless, appears quite sensitive to the details of the defect-charge representation in the narrow walls considered within the relatively small supercells accessible with the first-principles calculations.

Finally, all simulations predict that the polarization vectors in both neutral regions stay practically at the spontaneous value in the x direction, justifying the use of rather thin layers to represent them; this allows for a larger portion of the simulation box to be devoted to the region of interest. The wall itself is thicker than a neutral 180° domain wall [30]. In Fig. 3(b) we observe similar features close to the apex of the triangle as in the shell-model result in Fig. 2.

In general, there is a very good agreement between the shell-model and phase-field simulations. Both predict a zigzag wall within the charged region.

IV. DISCUSSION

A. One-dimensional character of domain-wall modulation

The simulations presented in the previous section are mostly done with two-dimensional simulation boxes (in the xy plane). However, simulations using three-dimensional supercells, typically $60\Delta \times 60\Delta \times 60\Delta$ in the phase-field simulations, were conducted as well: They systematically predict the development of a zigzag wall modulated along either the y or the z axis and constant along the other axis (the charged and neutral regions are stacked along the x direction). Hence, we conclude that the simulations using two-dimensional supercells describe the physics of the zigzag domain wall of interest. Notice that even though the modulation direction was observed to align only with a pseudocubic y or z direction, this does not need to be the case for all materials: The anisotropy of the transversal permittivity for the spontaneous state and the concrete form of the short-range interaction may lead to an alternative preferred wall-modulation direction (see the discussion below).

B. Origin of the zigzag profile of the wall

For the sake of gaining insight into the zigzag character of the wall, it is instrumental to use the simplified homogeneous-charge approximation, already used, e.g., in Fig. 3(a). It allows us to disregard the actual positions of the defects while preserving their average effect.

There is a simple reason why the domain wall cannot stay flat: In order for the bound-charge density due to the variation of solely P_x (recall that $\rho_{\mathbf{P}} = -\text{div}\mathbf{P}$) to approximately compensate the defect charge, the change in P_x between its spontaneous values would need to be approximately linear. Such a strong deviation from the spontaneous polarization in such a large volume region would cost too much energy.

In order to avoid the paraelectric state, the P_y component of polarization develops. A closer look at the polarization in Figs. 2 and 3 reveals that the $P_y = 0$ at the axis of the triangle. The P_y increases linearly along the direction of the y axis, and sharply drops in the region of the zigzag domain wall, thus being zero on average [see also Fig. 3(d)].

The visualization of how the ferroelectric polarization gives rise to bound charges $\rho_{\mathbf{P}} = -\text{div}\mathbf{P} = -(\frac{\partial P_x}{\partial x} + \frac{\partial P_y}{\partial y} + \frac{\partial P_z}{\partial z}) = \rho_{P_x} + \rho_{P_y} + \rho_{P_z}$ is depicted in Fig. 4 for the case with relatively small L , for which the effect is more pronounced. The upper panel shows the contribution to the polarization-originated bound charge from P_x . It is negative in the region of the zigzag wall (as it needs to be in a tail-to-tail wall), and zero elsewhere, i.e., P_x stays almost constant within the triangles. The middle panel depicts the contribution of the P_y component. Its linear increase along the y axis leads to a negative charge bound (blue in the triangular domain), while the sharp drop in the wall results in a large positive bound charge (red at the triangle edges). Adding these two [31] contributions

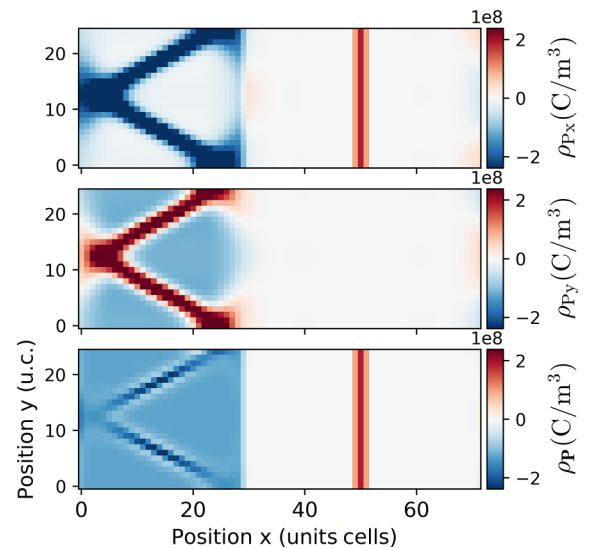


FIG. 4. Polarization-originated bound charges, stemming from the P_x (upper), P_y (middle) components of polarization, and their sum (bottom). For better visibility of the DW1 region we artificially reduce the intensity of charge in the DW2 by a factor of 10.

together (bottom panel) results in an almost constant negative bound charge within the entire charged region, which matches the positive compensation charge due to immobile defects. Notice that the $\rho_{\mathbf{P}}$ is not exactly constant in the wall region, but even there the differences (of lighter and darker areas) approximately cancel and lead to local electric fields only, which are energetically acceptable.

Thus, while the P_x component is responsible for the negative charge of the wall, P_y produces a positive and negative regions, which approximately compensates the negative wall and all the positive defect charges at the background. The polarization-originated bound charge approximately matches the defect charges, and there remain almost no sources of energetically costly electric fields.

Notice that the described mechanism of the balance between the bound and defect charges requires that the wall penetrate the whole thickness of the charged region, and therefore the height of the triangular domain must be approximately equal to L . Let us return back to the original question about the reason why the shape of the wall is zigzag. It is simply the shortest interface, which at the same time penetrates the whole charged layer. In other words, it is the energetically most economic wall from the perspective of the domain-wall surface energy density, which allows for the charge balancing mediated by variation of P_y .

A similar mechanism can be expected in cases where we deal with point charges instead of a homogeneous charge density: The variation of the electric field due to local charges averages out due to the large number of involved defects. Figure 3(c) demonstrates the robustness of the zigzag arrangement, which is present even for more strongly charged (and therefore more sparsely distributed) point defects.

Notice that the observed deviation of P_y costs energy; however, as this is a transversal deviation from the spontaneous vector, it costs less energy than the longitudinal deviation. This effect is related to the usually larger permittivity in the

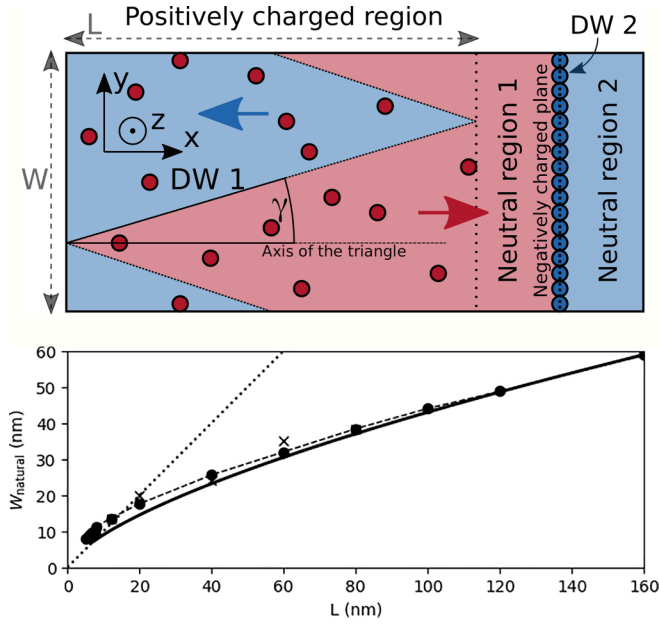


FIG. 5. Top: Schematic picture of the zigzag pattern, which is used in the derivation of $W_{\text{natural}}(L)$. Red and blue colors and arrows correspond here to positively and negatively oriented ferroelectric domains (with respect to the x axis). The color of the defects is as in Fig. 1. Bottom: Dependence of $W_{\text{natural}}(L)$. Bullets: Phase-field simulations with homogeneous compensation charge; the dashed line is just a connection of these. Crosses: Phase-field simulations with randomly distributed defect charges, as in Fig. 3(b). Solid line: Simplified model. The dotted line indicates dependence $W = L$, i.e., a triangle with identical width and height.

transversal than in the longitudinal direction in ferroelectrics [17,18].

C. Natural dimensions of triangular domains

So far, the dimensions W for the given L was chosen in such a way that it produces a more or less “acceptable” modulation length for the zigzag wall (i.e., a single triangle develops for each domain in the simulations). In the following we investigate how the energetically optimal base of the triangle W_{natural} depends on the width of the compensating charge distribution L .

We have used phase-field simulations to visualize the dependence in Fig. 5 (bottom panel). For the sake of the plot, the W_{natural} for each considered L (bullets and crosses in the figure) was evaluated as the W , for which the optimized configuration with one triangle in the simulation box has the lowest planar energy density in the yz plane. Thus, W_{natural} is the zigzag period, which would materialize as the energetically most favorable without constraints on W imposed by the y dimension of the simulation box.

To understand the behavior of $W_{\text{natural}}(L)$, and motivated by our simulations which systematically yield a zigzag profile independent of the actual positions of the defect charges, we use here again the homogeneous-defect-charge approximation, and the strictly triangular zigzag domain wall, as depicted in Fig. 5 (top panel). The first contribution to the planar energy density of the wall per unit area in the yz plane,

\mathcal{E}_1 , is the surface energy of the wall as a function of W and L ,

$$\mathcal{E}_1 = 2\mu\sqrt{\left(\frac{L}{W}\right)^2 + \frac{1}{4}}, \quad (1)$$

where μ represents the surface energy density of the wall. \mathcal{E}_1 grows with decreasing of W , because narrow triangular domains have a (relatively) large wall surface.

The second contribution to the energy density, \mathcal{E}_2 , accounts for the deviation of the polarization vector in the y direction from zero by $\Delta P_y(\mathbf{r})$. Let us assume that (i) the deviations ΔP_y are small enough and the Landau energy density f_L can be considered to be quadratic,

$$f_L = f_L(\mathbf{P}_s) + \alpha'_1(\Delta P_y)^2, \quad (2)$$

(ii) $\Delta P_y(\mathbf{r})$ linearly increases along y while P_x remains constant, (iii) the domain wall has zero thickness, and (iv) all other energy contributions, e.g., due to electric fields originating in incomplete compensation of the defect charge by the polarization variation, can be neglected. Under these assumptions, it can be derived that

$$\begin{aligned} \mathcal{E}_2 &= \frac{2}{W} \int_T f_L(P_{sx}, \Delta P_y, 0) - f_L(\mathbf{P}_s) d\mathbf{r} \\ &= \frac{4}{W} \int_0^L \left(\int_0^{x \tan(\gamma)} \frac{1}{2\chi_\perp} \left(\frac{2P_s y}{L} \right)^2 dy \right) dx \\ &= \frac{P_s^2 W^2}{12\chi_\perp L}. \end{aligned} \quad (3)$$

Here T is the area of a single triangle with the base W , $\chi_\perp = 1/(2\alpha'_1)$ represents the transversal susceptibility in the spontaneous ferroelectric state $\mathbf{P}_s = (P_{sx}, 0, 0)$, and 2γ is the angle at the triangle apex. In the derivation, we use the linear dependence of ΔP_y on y (with zero on the axis of the wedge),

$$\Delta P_y = \frac{2P_s}{L}y, \quad (4)$$

which allows for exact balancing of the homogeneous defect charge (the coefficient of proportionality is exactly equal to the homogeneous charge density in the charged layer). Therefore, the maximal ΔP_y found in the triangle is proportional to the width W of the triangle. From Eq. (3) it follows that \mathcal{E}_2 grows with increasing W , as sharper triangles require smaller maximal values of ΔP_y .

The total energy density of the wall per unit area in the yz plane is $\mathcal{E} = \mathcal{E}_1 + \mathcal{E}_2$. W_{natural} is the W for which the energy is minimal, requiring $d\mathcal{E}/dW = 0$. The complex nature of the \mathcal{E} does not allow one to express the $W_{\text{natural}}(L)$ analytically in a simple form; for large L the solution asymptotically approaches

$$W_{\text{natural}}(L) = \left(\frac{12\mu\chi_\perp L^2}{P_s^2} \right)^{1/3}. \quad (5)$$

The numerical solution is plotted in Fig. 5 (solid line), taking into account $\mu = 175 \text{ mJ/m}^2$, and $\chi_\perp = 279\epsilon_0$ evaluated from the utilized Landau potential $f_L(\mathbf{P})$ [32].

For large L the polarization will be close to the spontaneous one within the entire area of each triangle, and the adopted assumptions are largely valid, and the prediction of the simplified model agrees well with the numerical data. On the other hand, for small L we see a discrepancy between the numerical data and the predicted $W_{\text{natural}}(L)$. This is because the $\Delta\mathbf{P}_y(\mathbf{r})$ can no longer be considered small (see, e.g., Fig. 2), the volume of the wall itself becomes significant, and the adopted assumptions, in particular that of a constant P_x , are no longer satisfied. This will lead to smaller \mathcal{E}_2 , and thus to broader triangles obtained from simulations than is predicted by the theory, which indeed we observe in Fig. 5.

In general, a tendency to form narrow triangles (small γ) can be expected in materials with small planar energy density of the domain wall μ (small cost of the wall area), small spontaneous polarization magnitude P_s (small defect-charge volume density), small susceptibility χ_{\perp} (large energy cost due to induced transversal polarization $\Delta\mathbf{P}_y(\mathbf{r})$), and small background permittivity ε_B (reflecting contributions to the permittivity due to high-frequency polar modes and electronic degrees of freedom).

D. Deviations from the ideal zigzag pattern

As was already pointed out, there appear smokelike features at the tips of the triangles [see Figs. 2(b) and 3(b)]. These features are related to the somewhat smaller height of the wedge compared to the width of the charged region L , and they also develop as a response to the discrepancy between $W_{\text{natural}}(L)$ and the actual W (enforced by the y dimension of the simulation box), in particular when W is larger. To demonstrate this, we show an even more pronounced departure from the ideal zigzag pattern in Fig. 6, observed for triangles with increasing base W . The white regions in the figure represent small 90° domains with the ferroelectric polarization pointing along the $\pm y$ direction. Notice that the resulting 90° domain walls tend to form an angle of 45° with respect to the pseudocubic axes, i.e., they are close to mechanical compatibility [33].

For values of W smaller than W_{natural} the shape remains triangular, even though the overall wall length and hence its surface energy increase. This is because failure of the wall to percolate the complete thickness of the charged slab would be energetically forbidden, as explained above.

For values of W larger than W_{natural} the shape departs from triangular only very slowly, indicating a relatively large tolerance of the system to the change of the triangle width. At some point, the smokelike feature above the triangle grows larger, and is accompanied by smaller and larger cuts to the side of the triangle along its whole length. The actual positions of the cuts likely depend on the location of defect charges. For large W , the cut progressively separates the bottom part of the triangle, which becomes a seed for a second triangle, which will fully develop into another triangular domain for large enough W .

Let us point out that in a real situation the width of the triangles will likely depend on the history of the sample, and might be far from optimal. It will depend on, e.g., the number of seeds during the growth of the domain structure, on any pinning of the wall (influencing the ability of the triangles to

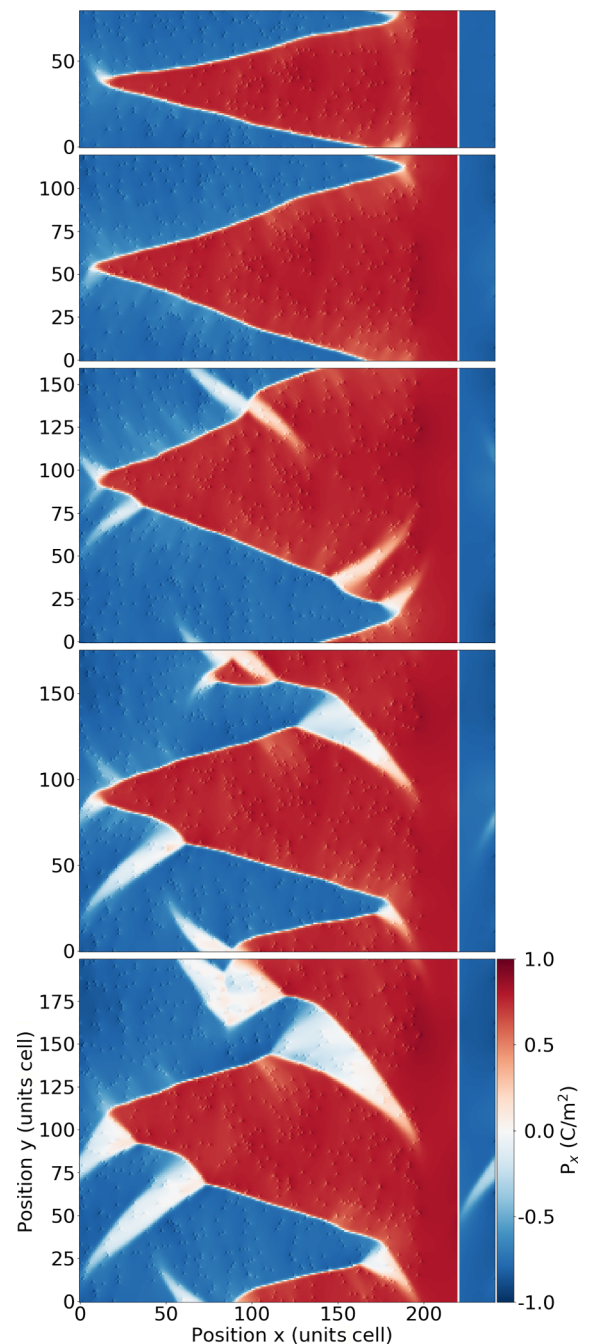


FIG. 6. Zigzag domain wall as obtained from mutually independent phase-field simulations for $L = 200\Delta = 80$ nm and $W \in \{0.80, 1.20, 1.60, 1.76, 2.00\} \times W_{\text{natural}}$. The color represents P_x . White regions are areas where the polarization is oriented along the y axis.

move, merge, or split), and on other aspects of the charged domain-wall formation. Thus, an irregular pattern and varying heights of the triangles can be expected.

The other situation for which the wall morphology strongly departs from the regular zigzag pattern appears for very small $L \lesssim 10\Delta$. Here the domain wall forms an irregular landscape within the limits of the charged region, utilizing the energetic advantage of crossing the oppositely charged defect in the wall center, if possible. We observed that in this case the wall

is pinned to the actual defect positions. The absence of the regular zigzag pattern is the reason why it was not possible to plot $W_{\text{natural}}(L)$ for small L in Fig. 5.

E. Theoretical and experimental context

The origin of the zigzag shape of ferroelectric charged domain walls was previously investigated theoretically by Zhang and coauthors in Ref. [12]. They construct a minimal Hamiltonian, including merely short-range and electrostatic interactions between electric dipoles, leading to the zigzag modulation of the uncompensated domain wall in a strictly uniaxial ferroelectric material.

Tikhonov and collaborators in Ref. [16] modeled uncompensated charged domain walls in the uniaxial ferroelectric $\text{Pb}_5\text{Ge}_3\text{O}_{11}$ using phase-field simulations, which led to a complex three-dimensional domain structure including mutual domain bifurcations. Compensation of the polarization bound charge by variation of the transverse polarization components was observed, which is a very similar mechanism to the one reported here.

The two aforementioned works [12,16] do not assume compensation of the charged wall by any extrinsic charge, which, apart from the fact that we work here with a multiaxial ferroelectric material, is the main difference compared to the study presented here. In contrast to Ref. [16] we do not prescribe the polarization on either side of the charged interface in any way.

An important distinctive feature of the zigzag pattern observed here from the previous theoretical studies which do consider compensation charge is that the domain wall here is practically independent of the actual positions of charged defects, i.e., the charges are not accumulated in the wall.

An experimental observation of a similar configuration of charged domain wall was recently reported in Ref. [4] for a 250-nm-thick BaTiO_3 film. Therein, a charged wall separates two regions with oppositely oriented polarization (perpendicular to the substrate). Triangular domains, which penetrate almost the entire film thickness, are observed along with smaller triangles. The 180° domain structure was seen to be dependent on the sample thinning and grounding of the electrodes. A comparable pattern was also observed in rhombohedral BiFeO_3 in Ref. [7]. There, a finely modulated zigzag wall forms within a larger-scale stripe motif. The structures of these walls bear a strong resemblance to the zigzag pattern studied here. A triangular charged domain interface (on a much larger scale) was also observed for LiNbO_3 [5].

Zigzag charged domain walls similar to those reported here are known to appear in magnetic thin films on scales of micrometers and larger [34–37]. Some of the triangles show similar smokelike features as those described here. The compensating electric charge used in the electrostatic considerations performed here is analogous to the notion of the magnetic charge due to orientation of the magnetization out

of the plane of the film. In this way, the magnetic charged wall can exist in thin films, while the out-of-plane component of the magnetization escapes the film and the magnetic flux closes outside the film.

V. CONCLUSIONS

We used atomistic shell-model and continuous phase-field simulations of doped ferroelectric PbTiO_3 to study the properties of 180° tail-to-tail domain walls that develop in spatially extended charge-compensation layers.

We observe that the charged domain walls systematically adopt a zigzag profile. We show that this pattern is stable against variations of compensating charge distribution and forms equally for point defect charges of different magnitude as well as for homogeneous charge distributions. We argue that the zigzag shape and triangular domains form as a consequence of the energetic demand to compensate the charged layer via polarization gradients while avoiding the paraelectric state, and keeping the surface area of the wall as small as possible. The former is achieved by polarization rotation, which we identify here as an efficient mechanism to distribute the uncompensated polarization bound charge from the wall over a larger area, and render the wall energetically more economic. Additionally, we provide a simplified expression for determining the natural width of the triangles W_{natural} , or equivalently the angle of the zigzag domain wall. For large enough thickness L of the charged slabs we found $W_{\text{natural}} \approx L^{2/3}$.

Although the charged region considered here was a slab with its normal aligned with the direction of spontaneous polarization in the surrounding domains, the physics presented here can be straightforwardly extended to more general orientations of the slab with respect to spontaneous polarization, and to non- 180° charged domain walls. This will be relevant, for example, for the slab normal along the pseudocubic axis in a rhombohedral ferroelectric, such as in BiFeO_3 .

The results presented here will be equally valid for the positively charged head-to-head wall, provided the compensation charges remain distributed in a sufficiently broad region and are immobile.

Thus, a finite slab of compensation defect charges should be perceived as a possible scenario to explain observations of nanoscale zigzag charged domain walls.

ACKNOWLEDGMENTS

The research was supported by Czech Science Foundation Grant No. 20-05167Y. Computational resources were provided by the e-INFRA CZ Project (ID:90140), supported by the Ministry of Education, Youth and Sports of the Czech Republic.

[1] J. Guyonnet, I. Gaponenko, S. Gariglio, and P. Paruch, *Adv. Mater.* **23**, 5377 (2011).

[2] G. Nataf, M. Guennou, J. Gregg, D. Meier, J. Hlinka, E. Salje, and J. Kreisel, *Nat. Rev. Phys.* **2**, 634 (2020).

- [3] J. Hlinka, M. Paściak, S. Körbel, and P. Marton, *Phys. Rev. Lett.* **119**, 057604 (2017).
- [4] T. Denneulin and A. Everhardt, *J. Phys.: Condens. Matter* **34**, 235701 (2022).
- [5] M. Schröder, A. Haußmann, A. Thiessen, E. Soergel, T. Woike, and L. Eng, *Adv. Funct. Mater.* **22**, 3936 (2012).
- [6] P. Bednyakov, T. Sluka, A. Tagantsev, D. Damjanovic, and N. Setter, *Sci. Rep.* **5**, 15819 (2015).
- [7] C.-L. Jia, L. Jin, D. Wang, S.-B. Mi, M. Alexe, D. Hesse, H. Reichlova, X. Marti, L. Bellaiche, and K. Urban, *Acta Mater.* **82**, 356 (2015).
- [8] T. Sluka, A. Tagantsev, P. Bednyakov, and N. Setter, *Nat. Commun.* **4**, 1808 (2013).
- [9] Z. Li, H. Wu, and W. Cao, *J. Appl. Phys.* **111**, 024106 (2012).
- [10] M. Y. Gureev, P. Mokry, A. K. Tagantsev, and N. Setter, *Phys. Rev. B* **86**, 104104 (2012).
- [11] Y. Watanabe, *Solid State Phenom.* **189**, 57 (2012).
- [12] J. Zhang, Y.-J. Wang, J. Liu, J. Xu, D. Wang, L. Wang, X.-L. Ma, C.-L. Jia, and L. Bellaiche, *Phys. Rev. B* **101**, 060103(R) (2020).
- [13] X. Wu and D. Vanderbilt, *Phys. Rev. B* **73**, 020103(R) (2006).
- [14] K. Rahmanizadeh, D. Wortmann, G. Bihlmayer, and S. Blügel, *Phys. Rev. B* **90**, 115104 (2014).
- [15] J. Sifuna, P. García-Fernández, G. S. Manyali, G. Amolo, and J. Junquera, *Phys. Rev. B* **101**, 174114 (2020).
- [16] Y. Tikhonov, J. R. Maguire, C. J. McCluskey, J. P. V. McConville, A. Kumar, H. Lu, D. Meier, A. Razumnaya, J. M. Gregg, A. Gruverman, V. M. Vinokur, and I. Luk'yanchuk, *Adv. Mater.* **34**, 2203028 (2022).
- [17] P. Ondrejko, P. Marton, M. Guennou, N. Setter, and J. Hlinka, *Phys. Rev. B* **88**, 024114 (2013).
- [18] T. Sluka, A. K. Tagantsev, D. Damjanovic, M. Gureev, and N. Setter, *Nat. Commun.* **3**, 748 (2012).
- [19] S. Tinte, M. Stachiotti, S. Phillpot, M. Sepiarsky, D. Wolf, and R. Migoni, *J. Phys.: Condens. Matter* **16**, 3495 (2004).
- [20] M. Sepiarsky and R. Cohen, *J. Phys.: Condens. Matter* **23**, 435902 (2011).
- [21] I. Todorov, W. Smith, K. Trachenko, and M. Dove, *J. Mater. Chem.* **16**, 1911 (2006).
- [22] P. Marton and J. Hlinka, *Phase Transitions* **79**, 467 (2006).
- [23] P. Ondrejko, P. Marton, V. Stepkova, and J. Hlinka, in *Domain Walls: From Fundamental Properties to Nanotechnology Concepts*, edited by D. Meier, J. Seidel, M. Gregg, and R. Ramesh (Oxford University Press, Oxford, 2020), Chap. 4, pp. 76–108.
- [24] Full parametrization of the Ginzburg-Landau-Devonshire model utilized here is $\alpha_1 = -5.42859 \times 10^8 \text{ J m C}^{-2}$, $\alpha_{11} = 4.78993 \times 10^8 \text{ J m}^5 \text{ C}^{-4}$, $\alpha_{12} = 1.13718 \times 10^9 \text{ J m}^5 \text{ C}^{-4}$, $\alpha_{111} = -5.47443 \times 10^7 \text{ J m}^9 \text{ C}^{-6}$, $\alpha_{112} = 1.44549 \times 10^7 \text{ J m}^9 \text{ C}^{-6}$, $\alpha_{123} = -5.87811 \times 10^8 \text{ J m}^9 \text{ C}^{-6}$, $\alpha_{1111} = -571565 \text{ J m}^{13} \text{ C}^{-8}$, $\alpha_{1112} = 6.04576 \times 10^7 \text{ J m}^{13} \text{ C}^{-8}$, $\alpha_{1122} = -1.78503 \times 10^8 \text{ J m}^{13} \text{ C}^{-8}$, $\alpha_{1123} = -1.59616 \times 10^8 \text{ J m}^{13} \text{ C}^{-8}$, $G_{11} = 1 \times 10^{-10} \text{ J m}^3 \text{ C}^{-2}$, $G_{12} = -1 \times 10^{-10} \text{ J m}^3 \text{ C}^{-2}$, $G_{44} = 1 \times 10^{-10} \text{ J m}^3 \text{ C}^{-2}$, $C_{11} = 3.26537 \times 10^{11} \text{ J m}^{-3}$, $C_{12} = 9.96364 \times 10^{10} \text{ J m}^{-3}$, $C_{44} = 6.96305 \times 10^{10} \text{ J m}^{-3}$, $q_{11} = 1.53698 \times 10^{10} \text{ J m C}^{-2}$, $q_{12} = 1.59913 \times 10^9 \text{ J m C}^{-2}$, $q_{23} = 5.79024 \times 10^9 \text{ J m C}^{-2}$, $\varepsilon_B = 1$.
- [25] P. Marton, A. Klíč, M. Paściak, and J. Hlinka, *Phys. Rev. B* **96**, 174110 (2017).
- [26] The ordinary strategy would be to fix the strain components e_{yy} , e_{zz} , and e_{yz} to the spontaneous values.
- [27] S. Nambu and D. A. Sagala, *Phys. Rev. B* **50**, 5838 (1994).
- [28] The simulation in Fig. 3(c) was conducted with z dimension of the simulation box equal to ten in order to allow for random distribution of charges in all directions and to avoid formation of chains of charges, as inevitably happens for two-dimensional simulation boxes.
- [29] The same observation is made for other phase-field simulations presented here, but it is not explicitly visualized.
- [30] B. Meyer and D. Vanderbilt, *Phys. Rev. B* **65**, 104111 (2002).
- [31] Notice that ρ_{Pz} is zero for two-dimensional simulation boxes.
- [32] The $f_L(P_{sx}, P_y, 0) = 1.65687 \times 10^8 + 2.02795 \times 10^8 P_y^2 + 4.15809 \times 10^8 P_y^4 - 1.62438 \times 10^7 P_y^6 - 5.71570 \times 10^5 P_y^8$.
- [33] J. Fousek and V. Janovec, *J. Appl. Phys.* **40**, 135 (1969).
- [34] S. Hamzaoui, M. Labrune, and I. Puchalska, *Appl. Phys. Lett.* **45**, 1246 (1984).
- [35] R. Engel-Herbert, D. Schaadt, S. Cherifi, E. Bauer, R. Belkhou, A. Locatelli, S. Heun, A. Pavlovska, J. Mohanty, K. Ploog *et al.*, *J. Magn. Magn. Mater.* **305**, 457 (2006).
- [36] C. Favieres, J. Vergara, and V. Madurga, *Materials* **13**, 4249 (2020).
- [37] H. Knüpfer and W. Shi, *Arch. Ration. Mech. An.* **239**, 1875 (2021).